

Detection of Slow Slip Events Using Wavelet Analysis of GNSS Recordings

Ariane Ducellier^{*1}, Kenneth C. Creager¹, and David A. Schmidt¹

ABSTRACT

At many places, tectonic tremor is observed in relation to slow slip and can be used as a proxy to study slow slip events of moderate magnitude in which surface deformation is hidden in Global Navigation Satellite System (GNSS) noise. However, in subduction zones in which no clear relationship between tremor and slow slip occurrence is observed, these methods cannot be applied, and we need other methods to be able to better detect and quantify slow slip. Wavelets methods such as the Discrete Wavelet Transform and the Maximal Overlap Discrete Wavelet Transform (MODWT) are mathematical tools for analyzing time series simultaneously in the time and the frequency domain by observing how weighted differences of a time series vary from one period to the next. In this article, we use wavelet methods to analyze GNSS time series and seismic recordings of slow slip events in Cascadia. We use detrended GNSS data, apply the MODWT transform, and stack the wavelet details over several nearby GNSS stations. As an independent check on the timing of slow slip events, we also compute the cumulative number of tremor in the vicinity of the GNSS stations, detrend this signal, and apply the MODWT transform. In both the time series, we can then see simultaneous waveforms for which timing corresponds to the timing of slow slip events. We assume that there is a slow slip event whenever there is a positive peak followed by a negative peak in the wavelet signal. We verify that there is a good agreement between slow slip events detected with only GNSS data and slow slip events detected with only tremor data for northern Cascadia. The wavelet-based detection method effectively detects events of magnitude higher than 6, as determined by independent event catalogs (e.g., Michel *et al.*, 2019). As a demonstration of using the wavelet analysis in a region without significant tremor, we also analyze GNSS data from New Zealand and detect slow slip events that are spatially and temporally close to those detected previously by other studies.

KEY POINTS

- We use a wavelet-based signal processing method to detect transients in GNSS data, such as slow slip events.
- In Cascadia, there is a good agreement between detections of slow slip using GNSS data and using tremor data.
- The method can be used as a starting point to identify slow slip without prior information, for example, New Zealand.

[Supplemental Material](#)

INTRODUCTION

Slow slip events are new phenomena discovered in the last two decades in many subduction zones, thanks to recordings of the displacement of Earth's surface by dense Global Navigation Satellite System (GNSS) networks (Schmidt and Gao, 2010; Vergnolle *et al.*, 2010; Jiang *et al.*, 2012; Wallace *et al.*, 2012). As with ordinary earthquakes, slow slip events represent

slip on a fault, for instance, the plate boundary between a tectonic plate subducting under another tectonic plate. However, they take a much longer time (several days to several years) to happen relative to ordinary earthquakes. They have a relatively short recurrence time (months to years) compared to the recurrence time of regular earthquakes (up to several hundreds of years), allowing scientists to observe and study many complete event cycles, which is typically not possible to explore with traditional earthquake catalogs (Beroza and Ide, 2011). A slow slip event on the plate boundary is inferred to happen when there is a reversal of the direction of motion at GNSS stations, compared to the secular interseismic motion. Slow

1. Department of Earth and Space Sciences, University of Washington, Seattle, Washington, U.S.A., <https://orcid.org/0000-0003-3668-9455> (AD); <https://orcid.org/0000-0003-4501-7415> (KCC)

*Corresponding author: ariane.ducellier.pro@gmail.com

Cite this article as Ducellier, A., K. C. Creager, and D. A. Schmidt (2022). Detection of Slow Slip Events Using Wavelet Analysis of GNSS Recordings, *Bull. Seismol. Soc. Am.* **XX**, 1–17, doi: [10.1785/0120210289](https://doi.org/10.1785/0120210289)

© Seismological Society of America

slip events have been observed at many places (Beroza and Ide, 2011; Audet and Kim, 2016), such as Cascadia (Bartlow, 2020), Nankai (Nishimura *et al.*, 2013), Alaska (Li *et al.*, 2016), Costa Rica (Jiang *et al.*, 2012), Mexico (Radiguet *et al.*, 2012), and New Zealand (Wallace, 2020).

At many places, tectonic tremor is also observed in relation to slow slip, but the spatial agreement between tremor and slow slip may vary along the strike of the plate boundary (Hall *et al.*, 2018). Tremor is a long (several seconds to many minutes), low-amplitude seismic signal with emergent onsets and an absence of clear impulsive phases. Tectonic tremors have been explained as a swarm of small, low-frequency earthquakes (LFEs; Shelly *et al.*, 2007), which are small-magnitude earthquakes ($M \sim 1$) for which frequency content (1–10 Hz) is lower than for ordinary earthquakes (up to 20 Hz). In subduction zones such as Nankai and Cascadia, tectonic tremor observations agree spatially and temporally with slow slip observations (Rogers and Dragert, 2003; Obara *et al.*, 2004). Because of this agreement, these paired phenomena have been called Episodic Tremor and Slip (ETS). However, this is not always the case. For instance, in northern New Zealand, tremor is more challenging to detect and seems to be located down-dip of the slow slip on the plate boundary (Todd and Schwartz 2016). In Alaska, the tremor zone only partially overlaps the long-term slow slip zone, and there does not appear to be any temporal agreement between tremor and slow slip occurrence (Wech, 2016).

In Cascadia, there are robust signals in both slow slip and tremor (Hawthorne and Rubin, 2013). This is also the case in Nankai (Hiramatsu *et al.*, 2008), where tiltmeters are used instead of GNSS. It is thus possible to use tremor as a proxy to observe slow slip events that are not directly observed in the GNSS data. For instance, Aguiar *et al.* (2009) studied 23 ETS events in Cascadia with more than 50 hr of tectonic tremor. For all these events, they computed both the Global Positioning System (GPS)-estimated moment release and the cumulative number of hours of tectonic tremor recorded. They observed a linear relationship between moment release and number of hours of tremor for slow slip events of moment magnitude 6.3–6.8. Based on this linear relationship, it is possible to infer the existence of smaller slow slip events of magnitude 5–6 occurring simultaneously with smaller tremor bursts of duration 1–50 hr occurring in between the big ETS events and for which there is no detectable signal in the GPS data.


Frank (2016) divided GPS time series observations from Cascadia and Guerrero, Mexico, into two groups; the first group contains days with abundant tremor and LFEs, the second group contains days when the number of tremor or LFEs is lower than a threshold. He then stacked separately the two groups of daily observations and observed a cumulative displacement in the direction corresponding to the loading period when few tremor or LFEs are observed and the surface deformation corresponds to the secular plate motion. He also observed a cumulative displacement in the opposite direction

corresponding to the release period when tremor and LFEs are observed. He was thus able to observe a reverse displacement corresponding to smaller slow slip events not directly observable in the GPS data for individual events.

However, these methods cannot be applied to detect slow slip events in places where tremor and slow slip occurrence are not well spatially and temporally correlated, tremor is not abundant, or the seismic network is not robust enough. We thus need other methods to be able to better detect and quantify slow slip.

Wavelet methods such as the Discrete Wavelet Transform (DWT) are mathematical tools for analyzing time series simultaneously in the time and the frequency domain by observing how weighted differences of a time series vary from one period to the next. Wavelet methods have been widely used for geophysical applications (e.g., Kumar and Fofoula-Georgiou, 1997). However, few studies have used wavelet methods to analyze recordings of slow slip, and their scope was limited to the detection of the bigger (magnitude 6–7) short-term (a few weeks) events (Szeliga *et al.*, 2008; Ohtani *et al.*, 2010; Wei *et al.*, 2012; Alba *et al.*, 2019).

Szeliga *et al.* (2008) determined the timing and the amplitude of 34 slow slip events throughout the Cascadia subduction zone between 1997 and 2005 using wavelets. They modeled the GPS time series by the sum of a linear trend, annual, and biannual sinusoids representing seasonal effects, heaviside step functions corresponding to earthquakes and hardware upgrades, and a residual signal. They then applied a Gaussian wavelet transform to the residual time series to get the exact timing of slow slip at each GPS station. The idea is that the wavelet transform allows us to analyze the signal both in the time and the frequency domains. A sharp change in the signal will be localized and seen at all time scales of the wavelet decomposition, contrary to what happens with the periodic sinusoids of the Fourier transform.


Instead of using wavelets in the time domain, Ohtani *et al.* (2010) used 2D wavelet functions in the spatial domain to detect slow slip events. They designed the Network  Filter to detect transient deformation signals from large-scale geodetic arrays. They modeled the position of the GPS station by the sum of the secular velocity, a spatially coherent field, site-specific noise, reference frame errors, and observation errors. The spatial displacement field is modeled by the sum of basis wavelets with time-varying weights. Their method has been successfully used to detect a transient event in the Boso peninsula, Japan, and a slow slip event in the Alaska subduction zone (Wei *et al.*, 2012).

Finally, Alba *et al.* (2019) used hourly water level records from four tide gauges in the Juan de Fuca Strait and the Puget Sound to determine relative vertical displacements associated with slow slip events between 1996 and 2011. Their main idea is that the tidal level measured at a given gauge is the sum of a noise component at multiple timescales (tides, ocean, and

atmospheric noise) and an uplift signal due to the slow slip events. The noise component is assumed to be coherent **2** between all tidal gauges, whereas the tectonic uplift signal is different provided that the gauges are far enough from each other. By stacking the tidal records after removing tides, the uplift signals cancel each other while the noise signal is amplified. By stacking the components at different time scales of the DWT decomposition, instead of stacking the raw tidal record, each of the components of the noise at different time scales is retrieved and can then be removed from the raw records to obtain the uplift signal. Because of the relative location of the tidal gauges at Port Angeles and Port Townsend compared to the slow slip region on the plate boundary, a slow slip event should result in uplift in Port Angeles (western part) and in subsidence in Port Townsend (eastern part). Indeed, the authors were able to clearly see a difference in the sign of the uplift at these two tidal gauges.

In our study, we use a similar approach to the previous studies with a different reasoning. We only stack signals at nearby GPS stations, assuming that the east–west displacement due to the slow slip events will then be the same at each of the GPS stations considered. We suppose that some of the noise component is different at each GPS station and will be eliminated by the stacking. Finally, we assume that the noise and the longitudinal displacement due to the slow slip events and the secular plate motion have different time scales, so that the wavelet decomposition will act as a band-pass filter to retrieve the displacement signal and highlight the slow slip events. We use wavelet methods to analyze GPS and tremor recordings of slow slip events in Cascadia. Our objective is to verify that there is a good agreement between slow slip events detected with only GNSS data and slow slip events detected with only tremor data. We thus want to demonstrate that the wavelet-based detection method can be applied to detect slow slip events that may currently be obscured using standard methods. Finally, we apply the method to GNSS data in New Zealand and successfully detect several slow slip events without needing to rely on the tremor data.

DATA

We first focused our study on northwest Washington State. For the GNSS data, we used the GPS time series provided by the Pacific Northwest Geodetic Array, Central Washington University. These are network solutions in ITRF2014 with phase ambiguities resolved with wide-lane phase biases. Orbits and satellite clocks provided by the Jet Propulsion Laboratory  NASA. North, east, and vertical directions are available. However, as the direction of the secular plate motion is close to the east direction, we only used the east direction of the GPS time series for the data analysis, as it has the best signal-to-noise ratio (SNR). The wavelet method works best with data with zero mean and no sharp discontinuities; so we use the cleaned dataset, that is GPS times series with linear trends, steps due to earthquakes

or hardware upgrades, and annual and semiannual sinusoids signals simultaneously estimated and removed following Szeliga *et al.* (2004). For the tremor data, we used the tremor catalog from the Pacific Northwest Seismic Network (PNSN; Wech, 2010).

For the application to slow slip events in New Zealand, we used the GPS time series provided by the Geological hazard information for New Zealand (GeoNet). The coordinates have been extracted by GeoNet during the GLOBK run from the combined daily solution files and converted to (east, north, and up) displacement in millimeters with respect to an a priori position and epoch in the ITRF2008 realization. The time series provided by GeoNet have no adjustments made to them, so they may, for example, contain offsets due to earthquakes, offsets due to equipment changes at individual sites, and seasonal (annual and semiannual) signals due to various causes. Here again, the direction of the secular interseismic plate motion is close to the West direction, so we only used the east–west component of the GPS time series for the data analysis. We detrended the data before applying the wavelet transform by carrying a linear regression of the whole time series and removing the straight line obtained from the regression.

METHOD

The maximal overlap DWT

The DWT is an orthonormal transform that transforms a time series $X_t(t = 0, \dots, N - 1)$ into a vector of wavelet coefficients $W_i(i = 0, \dots, N - 1)$. If we denote J the level of the wavelet decomposition, and the number of observations is equal to **4** $N = n * 2^J$, in which n is some integer greater than or equal to 1, the vector of wavelet coefficients can be decomposed into J wavelet vectors W_j of lengths $\frac{N}{2}, \frac{N}{4}, \dots, \frac{N}{2^j}$ and one scaling vector V_J of length $\frac{N}{2^J}$. Each wavelet vector W_j is associated with changes on time scale $\tau_j = dt2^{j-1}$, in which dt is the time step of the time series and corresponds to the filtering of the original time series with a filter with nominal frequency interval $[\frac{1}{dt2^{j+1}}; \frac{1}{dt2^j}]$. The scaling vector V_J is associated with averages in time scale $\lambda_J = dt2^J$ and corresponds to the filtering of the original time series with a filter with nominal frequency interval $[0; \frac{1}{dt2^{J+1}}]$. Wavelet vectors can be further decomposed into details and smooths, which are more easily interpretable. We define for $j = 1, \dots, J$ the j th wavelet detail D_j , which is a vector of length N , and is associated to time scale $\tau_j = dt2^{j-1}$. Similarly, we can define for $j = 1, \dots, J$ the j th wavelet smooth S_j , which is a vector of length N , and is associated to scales $\tau_{j+1} = dt2^{j+1}$ and higher. The basic idea is to reapply to W_j the wavelet filter that was used to construct W_j from the initial time series X . Together, the details and the smooths define the multiresolution analysis (MRA) of X : **5**

$$X = \sum_{j=1}^J D_j + S_J. \quad (1)$$

The DWT presents several disadvantages. First, the length of the time series must be a multiple of 2^j in which j is the level of the DWT decomposition. Second, the time step of the wavelet vector W_j is $dt2^j$, which may not correspond to the time when some interesting phenomenon is visible on the original time series. Third, when we circularly shift the time series, the corresponding wavelet coefficients, details, and smooths are not a circularly shifted version of the wavelet coefficients, details, and smooths of the original time series. Thus, the values of the wavelet coefficients, details, and smooths are strongly dependent on the time when we start experimentally gathering the data. Finally, when we filter the time series to obtain the details D_j and smooths S_j , we introduce a phase shift that makes it difficult to line up meaningfully the features of the MRA with the original time series.

To overcome the disadvantages described above, we use instead the Maximal Overlap Discrete Wavelet Transform (MODWT). The MODWT transforms the time series $X_t(t = 0, \dots, N - 1)$ into J wavelet vectors $\tilde{W}_j(j = 1, \dots, J)$ of length N and a scaling vector \tilde{V}_J of length N . As is the case for the DWT, each wavelet vector \tilde{W}_j is associated with changes on scale $\tau_j = dt2^{j-1}$ and corresponds to the filtering of the original time series with a filter with nominal frequency interval $[\frac{1}{dt2^{j+1}}; \frac{1}{dt2^j}]$. The scaling vector \tilde{V}_J is associated with averages in scale $\lambda_j = dt2^j$ and corresponds to the filtering of the original time series with a filter with nominal frequency interval $[0; \frac{1}{dt2^{j+1}}]$. As is the case for the DWT, we can write the MRA:

$$X = \sum_{j=1}^J \tilde{D}_j + \tilde{S}_J. \quad (2)$$

The MODWT of a time series can be defined for any length N . The time step of the wavelet vectors \tilde{W}_j and the scaling vector \tilde{V}_J is equal to the time step of the original time series. When we circularly shift the time series, the corresponding wavelet vectors, scaling vector, details, and smooths are shifted by the same amount. The details and smooths are associated with a zero phase filter, making it easy to line up meaningfully the features of the MRA with the original time series. The wavelet methods for time series analysis are explained in a more detailed way in (Percival and Walden, 2000).

The boundary conditions at the two edges of the time series will affect the wavelet coefficients. For the MODWT, if we denote L the length of the base wavelet filter used for the wavelet decomposition (in our study, we used a Least Asymmetric wavelet filter of length $L = 8$, see Percival and Walden, 2000, section 4.8, page 107), the length of the wavelet filter at level j used to compute the wavelet detail D_j is:

$$L_j = (2^j - 1)(L - 1) + 1. \quad (3)$$

The wavelet coefficients of the detail at level j affected by the boundary conditions at the edges would then be the coefficients

with indices $t = 0, \dots, L_j - 2$ or $t = N - L_j + 1, \dots, N - 1$ (see Percival and Walden, 2000, section 5.11, page 199). We get $L_j = 442$ for $j = 6$, $L_j = 890$ for $j = 7$ and $L_j = 1786$ for $j = 8$. In practice, the part of the wavelet details affected by the boundary conditions is much shorter than that. We compared the wavelet details computed when using only the data between 2008 and 2012 and the wavelet details computed when using the entire time series from 2000 to 2021 (Fig. S1, available in the supplemental material to this article). Even at level 8 only about 6 months of data on each side are affected by the boundary conditions.

Application to synthetic data

To illustrate the wavelet transform method, we first apply the MODWT to synthetic data. Because slow slip events occur in Cascadia on a regular basis, every twelve to eighteen months, we create a synthetic signal of period $T = 500$ days. To reproduce the ground displacement observed on the longitudinal component of GPS stations in Cascadia, we divide each period into two parts: In the first part of duration $T - N$, the displacement is linearly increasing and corresponds to the inter seismic plate motion in the eastern direction; in the second part of duration N , the displacement is linearly decreasing and corresponds to a slow slip event on a reverse fault at depth triggering a ground displacement in the western direction. To see the effect of the duration of the slow slip event, we use different values for $N = 5, 10, 20, 40$ days. The amplitude of the set is normalized to 1. Figure 1 shows the synthetics, the details D_j of the wavelet decomposition for levels 1–10, and the smooth S_{10} for the four durations of a slow slip event.

The ramp-like signal is transformed through the wavelet filtering into a waveform with first a positive peak and then a negative peak. The shape of the waveform is the same for every level of the wavelet decomposition, but the width of the waveform increases with the scale level. For the 8th level of the wavelet decomposition, the width of the waveform is nearly as large as the time between the two events. At larger scales, the waveforms start to merge two contiguous events together and make the wavelet decomposition less interpretable. For an event of duration 5 days, the wavelet details at levels higher than 3 have a larger amplitude than the wavelet details at lower scales. For an event of duration 10 days, the wavelet details at levels higher than 4 have a larger amplitude than the wavelet details at lower scales. For an event of duration 20 days, the wavelet details at levels higher than 5 have a larger amplitude than the wavelet details at lower scales. For an event of duration 40 days, the wavelet details at levels higher than 6 have a larger amplitude than the wavelet details at lower scales. Thus, the scale levels at which an event is being seen in the wavelet details give us an indication about the duration (and the magnitude) of the slow slip event. The big slow slip events of magnitude 6–7 typically trigger a signal that lasts about one week at an individual GPS station, and the whole event lasts several

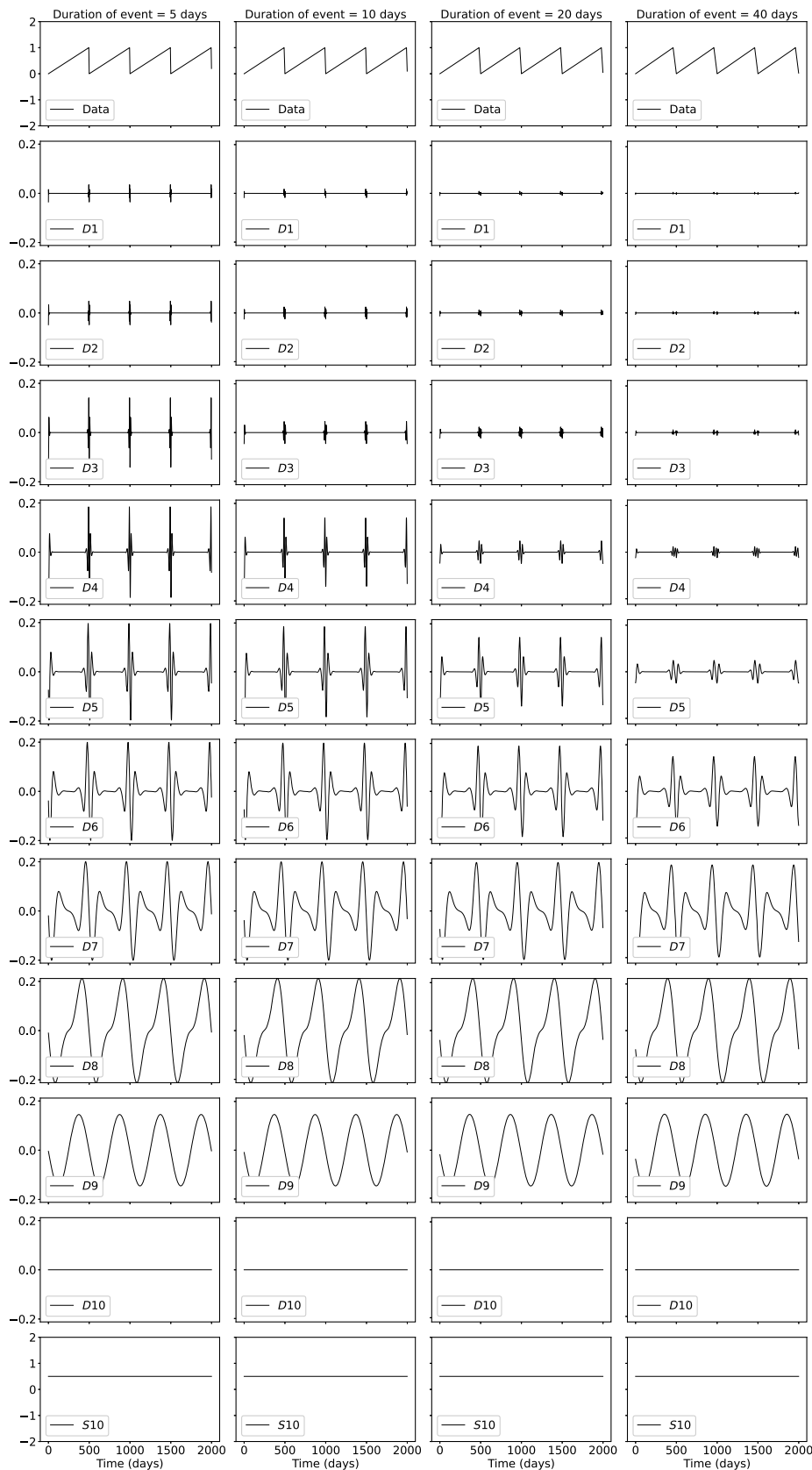
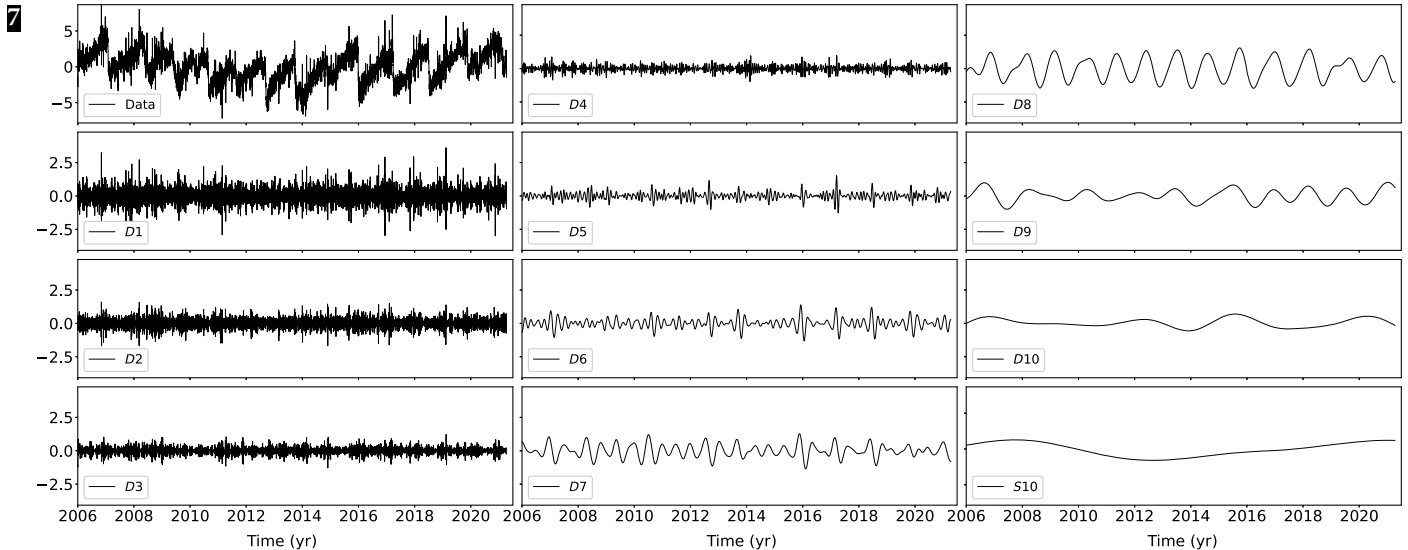


Figure 1. Demonstration of a wavelet decomposition for a synthetic dataset. A synthetic time series is created (top row) with steps of period 500 days, and transient durations of 2 days (left), 5 days, 10 days, and 20 days (right). The resulting details and smooths are shown in increasing level. The amplitude of the synthetic time series is normalized to 1, and the details and smooths show the relative amplitude.

weeks. We expect them to start being visible at the level 5 of the wavelet decomposition but to not be noticeable at lower time scales.

MODWT of GPS and tremor data

The DWT and MODWT methods must be used on a continuous time series, without gaps in the recordings. To deal with the gaps in the GNSS recordings, we simply replace the missing values by interpolation. The value for the first day for which data are missing is equal to the mean of the five days before the gap. The value for the last day for which data are missing is equal to the mean of the five days after the gap. The remaining missing values are computed by doing a linear interpolation of the first and the last values and adding a Gaussian noise component with mean zero and standard deviation equal to the standard deviation of the whole time series. We verify how the wavelet details may be affected by looking at a GPS time series without missing values, and compared the wavelet details with and without removing some data points. Station PGC5 recorded continuous 1390 days between 2009 and 2013 without any missing values. We first computed the wavelet details without missing values. Then, we removed ten neighboring values, replaced them using the method described earlier (linear interpolation plus Gaussian noise), and computed the wavelet details with the replaced values. Figure S2 shows a comparison of the two wavelet details for two different locations of the missing



values. We can see that there are visible differences in the time series itself and in the details at the smallest levels of the wavelet decomposition. However, the differences between the wavelet details with and without missing values get smaller and smaller with increasing levels of details, and are barely visible for the levels that are the most relevant (levels 6 and above). We thus conclude that we can easily replace the missing values in the GNSS time series without introducing false detections of slow slip events.

We then applied the wavelet filtering to real GPS data. Figure 2 shows the longitudinal displacement for GPS station PGC5, located in southern Vancouver Island, the details of the wavelet decomposition for levels 1–8, and the smooth. In the data, we can see a sharp drop in displacement whenever there is a documented slow slip event. For levels 5–8, which correspond to time scales 16, 32, 64, and 128 days, we can see in the details a positive peak followed by a negative peak whenever there is a drop in displacement in the data. We thus verify that the wavelet method can detect steps in the time series associated with slow slip events.

To increase the SNR and better detect slow slip events, we stack the signals from several neighboring GPS stations. We choose to focus on GPS stations located close enough to the tremor zone to get a sufficiently high amplitude of the slow slip signal. We choose 16 points along the 40 km depth contour of the plate boundary (model from Preston *et al.*, 2003) with spacing equal to 0.1° in latitude (red triangles on Fig. 3). Then we took all the GPS stations located in a 50 km radius for a given point, compute the wavelet details for the longitudinal displacement of each station, and stack each detail over the GPS stations. We thus have a stacked detail for each level 1–10 of the wavelet decomposition.

To assess the success of the wavelet decomposition for detecting slow slip events in GPS time series, we validate the approach by comparing to an independent proxy for slow

Figure 2. Top left: east–west displacement recorded at Global Positioning System (GPS) station PGC5. The resulting details and smooth of the wavelet decomposition are shown in increasing level from top to bottom and from left to right.

slip events. We took all the tremor epicenters located within a 50 km radius centered on one of the 16 locations marked by red triangles on Figure 3. Then we computed the cumulative number of tremor within this circle. Finally, we removed a linear trend from the cumulative tremor count and applied the wavelet transform. Because of the preprocessing applied to the tremor data before that wavelet transform, the measurement unit associated with the corresponding wavelet details is the fraction of tremor in a day divided by the total number of days. The average value is 1 divided by the total number of days. Figure 4 shows an example of the wavelet decomposition for the third northernmost location on Figure 3 (which is the closest to GPS station PGC5). Contrary to what happens for the GPS data, we see a sharp increase in the time series whenever there is a tremor episode, which translates into a negative peak followed by a positive peak in the wavelet details.

APPLICATION TO DATA FROM CASCADIA

We stacked the 8th level detail of the wavelet decomposition of the displacement over all the GPS stations located in a 50 km radius of a given point, for the 16 locations indicated in Figure 3. The result is shown in the top panel of Figure 5, in which each line represents one of the locations along strike. To better highlight the peaks in the wavelet details, we highlighted in red the time intervals in which the amplitude of the stacked detail is higher than a threshold and in blue the time intervals in which the amplitude of the stacked detail is lower than minus the threshold. To compare the GPS signal with the tremor signal, we plotted the 8th level detail of the wavelet

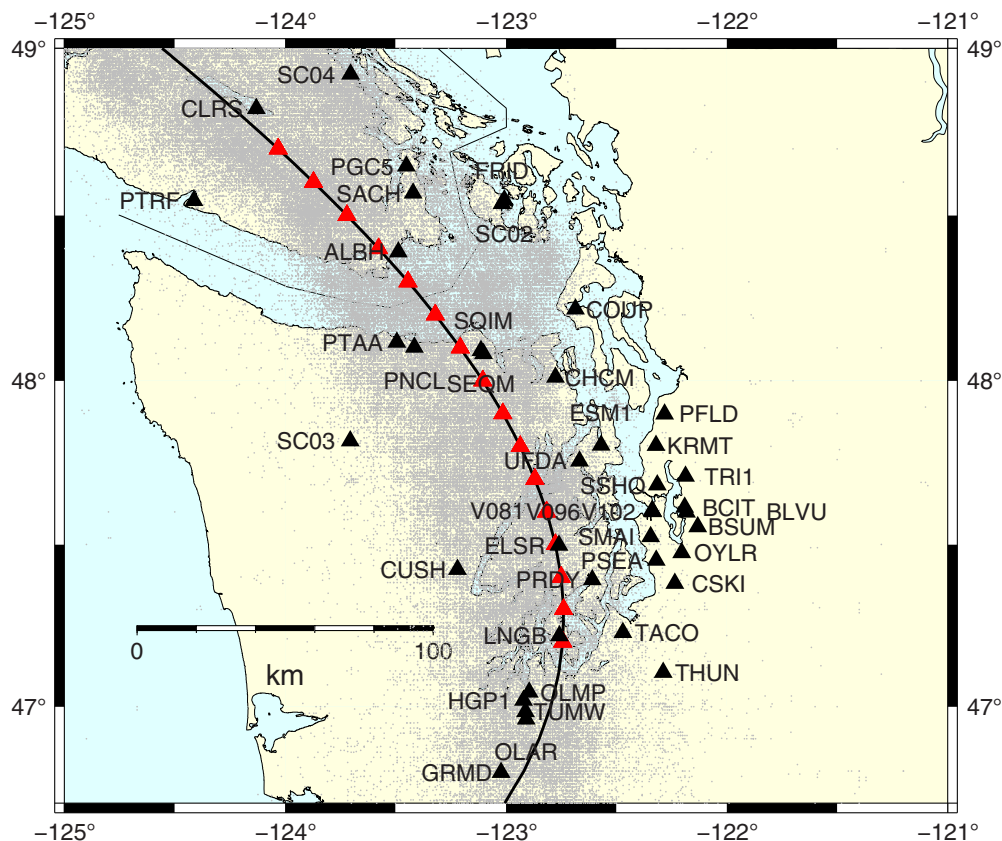


Figure 3. GPS stations used in this study (black triangles). The black line represents the 40 km depth contour of the plate boundary model by [Preston et al. \(2003\)](#). The red triangles are the locations where we stack the GPS data. The small gray dots are all the tremor locations from the Pacific Northwest Seismic Network (PNSN) catalog. The color version of this figure is available only in the electronic edition.

decomposition of the tremor count on the bottom panel of Figure 5. We multiplied by -1 the cumulative tremor count for the wavelet decomposition in order to be able to match positive peaks with positive peaks and negative peaks with negative peaks. In the tremor catalog from the PNSN, there are 17 tremor events with more than 150 hr of tremor recorded. The events are summarized in Table 1. The time of the event is the start date plus half the duration of the event.

Although the latitudinal extension of the events is not always the same for the GPS data and for the tremor data, we identify the same 13 events in both the 8th wavelet decompositions for the 8th level: January 2007, May 2008, May 2009, August 2010, August 2011, September 2012, September 2013, August–November 2014, January 2016, March 2017, June 2018, March–November 2019, and October 2020–January 2021. Although there are two events in the tremor catalog in August 2014 and November 2014, these two events are not distinguishable in the 8th level details and look more like a single event slowly propagating from South to North. The same phenomenon is observed in 2019 when two tremor events in March and November 2019 are merged into a single

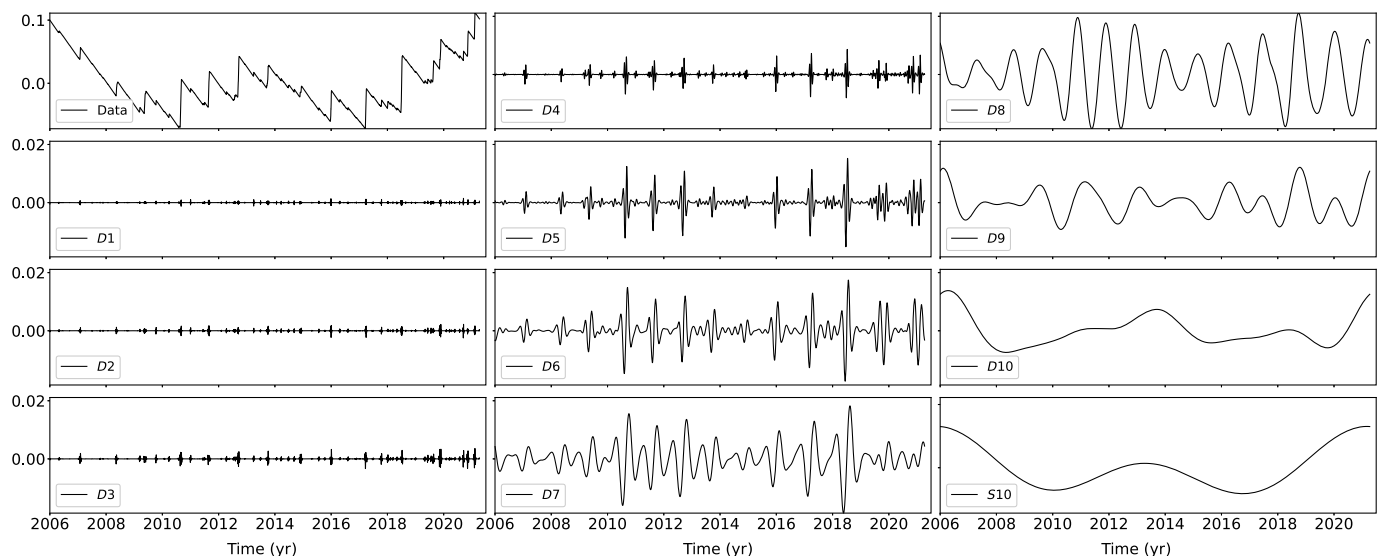
event propagating slowly from south to north. In 2020–2021, the wavelet decomposition of the tremor shows one event in the south in October–November 2020 and one event in the North in January 2021, but these three events look like a single event propagating slowly from south to north in the wavelet decomposition of the GPS data.

A similar comparison is shown for the wavelet decomposition of the GPS data and the wavelet decomposition of the tremor count data for the 7th level and the 6th level, respectively (Figs. 6 and 7). The events are harder to see in the 7th level than in the 8th level, both for the GPS data and the tremor count data. The wavelet decomposition is more noisy for the GPS data between 2010 and 2012, but it does not seem that there are more slow slip events visible in the 7th level.

For the 6th level detail, we see an additional event in the south in Fall 2009 that is

present both in the GPS and the tremor data. It may correspond to the northern extent of a big ETS event occurring in Fall 2009 south of the study area (event 19 in the [Michel et al., 2019](#) catalog). There are three small signals in the GPS data in Winter 2012, Fall 2017, and Winter 2020 that are not present in the tremor data and may be false detections. To summarize, we assume that robust detections are events present in both GPS and tremor time series, and false detections are events present in the GPS but not in the tremor time series. Then, all the 13 events present on the 8th level detail of the wavelet decomposition are robust detections, and 14 of the 17 events present on the 6th level detail of the wavelet decomposition are robust detections.

To better evaluate the number of robust and false detections, we convert the wavelet details into trinary time series. If the absolute value of the wavelet detail is higher than a threshold, we replace the value by 1 (for positive values) or -1 (for negative values); otherwise we replace the value by 0. We do this on both the wavelet details of the GPS data and of the tremor data. Then we decide that if both the GPS and the tremor time series take the value 1 (or both take



the value -1), we have a robust detection (true positive, TP). If the GPS and the tremor time series have opposite signs, or if the absolute value of the GPS time series is 1 but the value of the tremor time series is 0, we have a false detection (false positive, FP). If both the time series take the value 0, we do not have detection (true negative, TN). If the GPS time series take the value 0, but the absolute value of the tremor time series is 1, we miss a detection (false negative, FN). We then define the sensitivity (true positive rate) and the specificity (equal to 1 minus the false positive rate) as:

$$\text{Sensitivity} = \frac{\text{TP}}{\text{TP} + \text{FN}} \quad \text{Specificity} = \frac{\text{TN}}{\text{TN} + \text{FP}}. \quad (4)$$

We can then evaluate the quality of the detections obtained with our method by plotting a receiver operating characteristic curve (ROC curve). The ROC curve is widely used for binary classification problems in statistics and machine learning. We calculate an ROC value by varying the values of the threshold (here the two thresholds used to convert the GPS and the tremor time series into trinary time series), computing the corresponding values of the true positive rate and the false positive rate (equal to 1 minus the specificity), and plotting the true positive rate as a function of the false positive rate. If the classification was made randomly, all the points would fall on the first diagonal. If the classifier was perfect, the corresponding point would fall on the top left corner of the graph with true positive rate equal to 1 and false positive rate equal to 0. The bigger the area under the curve, the better the classification method is.

Because the slow slip events are better seen on levels 6, 7, and 8 of the wavelet decomposition, we first add the wavelet details corresponding to levels 6–8, and transform the resulting time series into a trinary time series. We apply this transform to both the GPS and the tremor time series with varying

Figure 4. Details and smooth of the wavelet decomposition of the detrended cumulative tremor count around the third northernmost red triangles on Figure 3 (latitude 48.5).

thresholds. We then plot the ROC curve on Figure 8, each dot representing a different threshold. The corresponding sums of the wavelet details for the GPS data and the tremor data are shown on Figure 9. We can see that there is a trade-off between sensitivity and specificity as we vary the threshold. If we decrease the false positive rate, we also decrease the number of true events detected. If we increase the number of true events detected, we also increase the false positive rate. If we increase the threshold for the tremor, the curve goes farther away from the first diagonal, that is, we get better classification results. If we increase the threshold for the GPS, the false positive rate and the number of events detected decrease. In Figure 9, we have chosen thresholds for the GPS time series and the tremor time series such that the specificity is higher than 0.75 (that is the false positive rate is lower than 0.25), and the sensitivity is the highest possible, that is we have chosen the thresholds corresponding to the dot that is the farthest from the diagonal, which is random.

In addition to the magnitude 6 events discussed earlier, Michel *et al.* (2019) have also identified several magnitude 5 events using a variational Bayesian Independent Component Analysis (vbICA) decomposition of the signal. Because we expect smaller magnitude events to be more visible at smaller time scales of the wavelet decomposition (level 5), we verify for all these events whether a signal can be seen at the same time as the time given in their catalog. Most of these magnitude 5 events are also subevents of bigger magnitude 6 events. Table 2 summarizes for each event its timing, its number, and its magnitude, as indicated in the catalog from Michel *et al.* (2019), and whether it is part of a bigger magnitude 6 event.

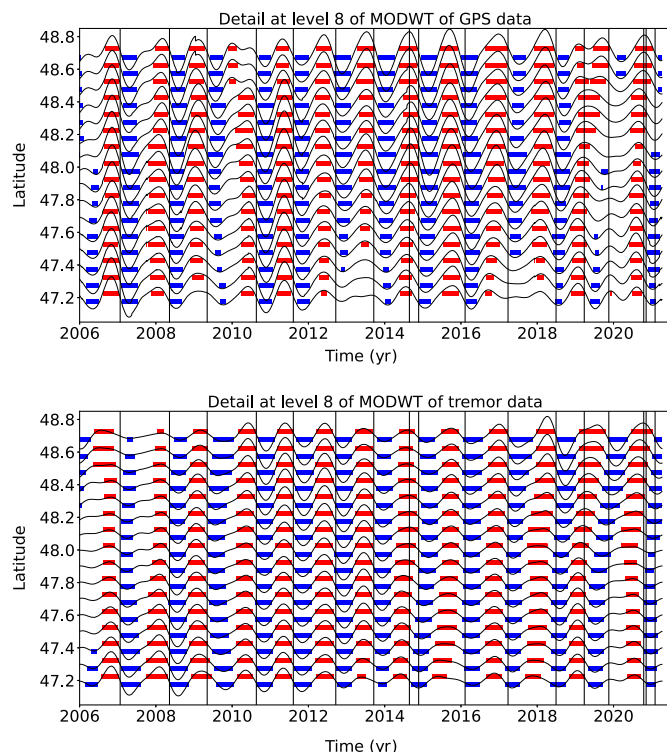


Figure 5. Top: Stacked 8th level details of the wavelet decomposition of the displacement over all the GPS stations located in a 50 km radius of a given point for the 16 red triangles indicated in Figure 3. Bottom: 8th level detail multiplied by -1 of the cumulative tremor count in a 50 km radius of a given point for the same 16 locations. The black lines represent the timings of the Episodic Tremor and Slip (ETS) events from Table 1. We mark by a red rectangle every time in which the amplitude is higher than a threshold of 0.4 mm (for the GPS) or 0.003 (for the tremor, that is about 17 times the average value of the signal). We mark by a blue rectangle every time in which the amplitude is lower than minus the threshold. The color version of this figure is available only in the electronic edition.

Figure 10 shows the 5th level detail wavelet decomposition of the GPS data. The red lines show the timing of the big slow slip events from Table 1, and blue lines show the timing of the small slow slip events from Table 2.

All the 14 events that are subevents of a bigger event are visible at level 5. However, this may be because the bigger events are clearly seen at levels 6–8 and also at smaller time scales. The one small event that is not part of a bigger event (Winter 2009) is visible at level 5 of the wavelet decomposition. However, some other events that are not in the catalog of Michel *et al.* (2019)'s catalog are also visible in late 2007, early 2010, early 2012, and early 2020. Therefore, it is difficult to differentiate between a robust detection and a false detection, and to conclude whether the method can indeed detect events of magnitude 5.

In Figure 9, we see four smaller events that are not in the catalog of Michel *et al.* (2019): at about 2007.5, there is a negative peak followed by a positive peak (that is an event in the

TABLE 1
Episodic Tremor and Slip events with $M > 6$ Identified by Maximal Overlap Discrete Wavelet Transform (MODWT) in Both the Global Positioning System (GPS) and the Tremor Data

Time	Duration (days)	Number of Tremor (hr)	Event Number	Magnitude
2007.06	28	398	3	6.68
2008.36	25	402	10	6.56
2009.35	24	248	16	6.49
2010.63	29	518	24	6.54
2011.60	37	479	30	6.47
2012.72	37	620	34	6.54
2013.71	27	423	41	6.58
2014.65	15	190	48	6.03
2014.89	38	385	51	6.40
2016.11	43	421	54	6.79
2017.23	19	279	59	6.61
2018.49	22	381		
2019.23	34	195		
2019.88	16	205		
2020.79	26	193		
2020.86	12	162		
2021.09	14	230		

The duration and the number of tremor are from the tremor catalog of the Pacific Northwest Seismic Network (PNSN). The event number and the magnitude are from the slow slip catalog of Michel *et al.* (2019).

opposite direction of what would be expected from slow slip) at about 2010.2, 2012.2, and 2020.2; there are positive peaks followed by negative peaks for all the sixteen locations studied in this article. These events are highlighted in Figure S4. Looking back at the original GPS data, there is a small increase in the displacement in the eastern direction that lasts about one or two months at about 2007.5. However, the direction of the displacement does not correspond to a slow slip event, and another cause should be found to explain this signal. There is a decrease in displacement that lasts several months at about 2010.2. This transient may correspond to a long-duration slow slip event. There is a small decrease in displacement at about 2012.2. Its amplitude is small, but the duration and direction correspond to a slow slip event, so this transient could be a very small slow slip event. Finally, there is also a small decrease in displacement at about 2020.2 that is difficult to interpret.

Because of the short distances between the GPS stations and the locations of the red triangles on the map from Figure 3, the same station could be used multiple times for the stacking at different locations. When considering two different locations, the stacking is thus made over an overlapping number of stations. Table 3 summarizes the number of stations and the number of overlapping stations for each location on Figure 3. We hypothesize that the small displacement in the eastern direction seen at about 2007.5 could be due to a misbehaving station common to several locations. However, several GPS stations

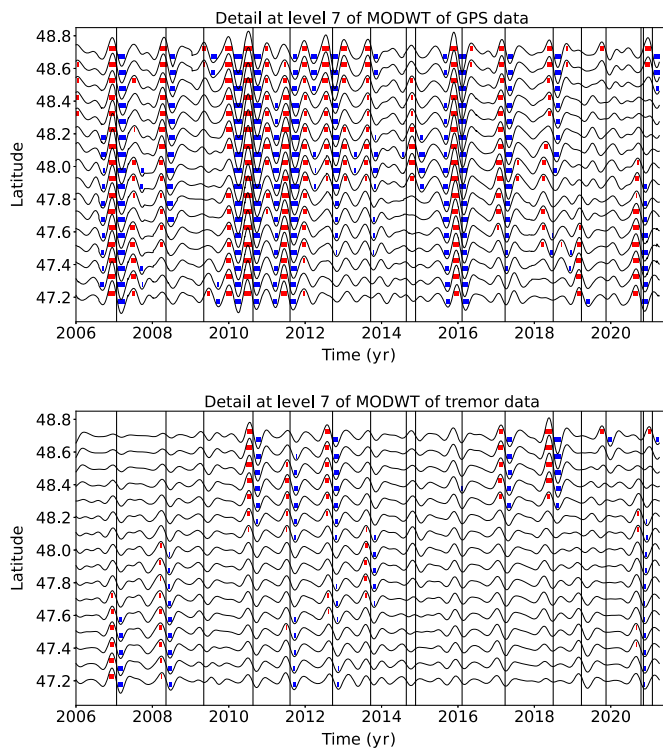


Figure 6. Top: Stacked 7th level details of the wavelet decomposition of the displacement over all the GPS stations located in a 50 km radius of a given point for the 16 red triangles indicated in Figure 3. Bottom: 7th level detail multiplied by -1 of the cumulative tremor count in a 50 km radius of a given point for the same 16 locations. The black lines represent the timings of the ETS events from Table 1. We mark by a red rectangle every time in which the amplitude is higher than a threshold of 0.5 mm (for the GPS) or 0.01 (for the tremor that is about 56 times the average value of the signal). We mark by a blue rectangle every time in which the amplitude is lower than minus the threshold. The color version of this figure is available only in the electronic edition.

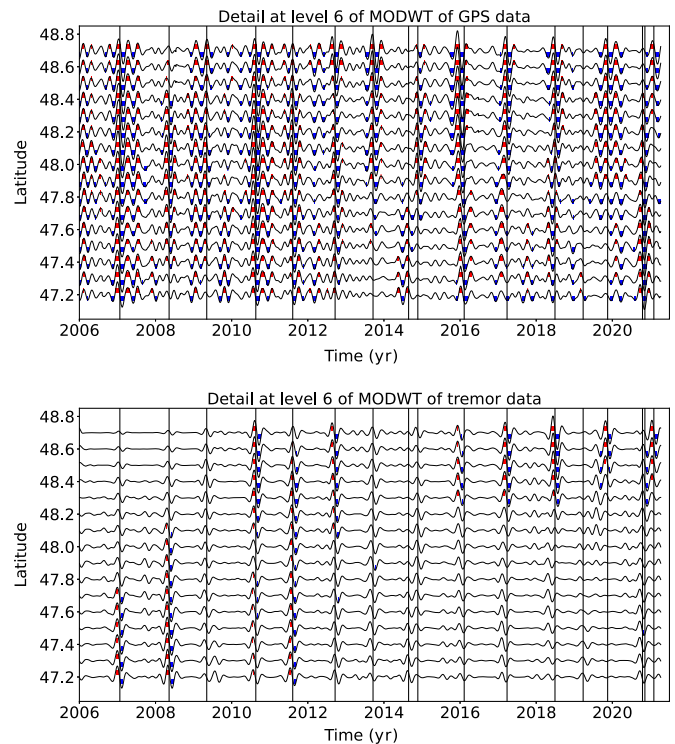


Figure 7. Top: Stacked 6th level details of the wavelet decomposition of the displacement over all the GPS stations located in a 50 km radius of a given point for the 16 red triangles indicated in Figure 3. Bottom: 6th level detail multiplied by -1 of the cumulative tremor count in a 50 km radius of a given point for the same 16 locations. The black lines represent the timings of the ETS events from Table 1. We mark by a red rectangle every time in which the amplitude is higher than a threshold of 0.3 mm (for the GPS) or 0.009 (for the tremor that is about 51 times the average value of the signal). We mark by a blue rectangle every time in which the amplitude is lower than minus the threshold. The color version of this figure is available only in the electronic edition.

indeed show an increase in the displacement in the eastern direction at about 2007.5. There are many missing data around that time, so it is difficult to conclude.

Another possibility is that common mode signals could stack constructively across GNSS stations and produce peaks in the wavelet details that are actually due to nontectonic signals. We computed common mode signals for different latitude bins (Each bin has width equal to half-a-degree of latitude.) following the same method as [Nuyen and Schmidt \(2021\)](#). We first stacked all the time series for the stations in each latitude bin that are located more than 100 km east of the 40 km depth contour of the plate boundary. We assume that these stations are not sensitive to the deformation on the plate interface. We then apply a yearly moving average to each common mode signal to remove any leftover noise. The common mode signal was then removed from the GNSS time series depending on each site's latitude. Figure S3 shows the corresponding sum of the stacks of the 6th, 7th, and 8th wavelet details obtained from the resulting time series. The common modes seem to have little impact

on the results and do not explain the additional four small events that we noted in Figure 9.

convert our filtered eastward displacement time series into a slow slip event catalog. note that red bars represent displacements exceeding a threshold of 0.8 mm (east) and blue marks displacements less than minus -0.8 mm (west). During times with no slow slip stations on the overriding plate are pushed slowly eastward by the locked subducting plate. Slow slip events represent GPS motion toward the west. Thus, we infer that slow slip events happen when red bars are immediately followed by blue bars in the wavelet details. We have identified everywhere that this has happened, and mark it with a green line in Figure 11 and as a row in Table 4. We find 17 possible SSEs by this method using filtered GPS data only. For each of these 17 events we determine the time difference between the mid time of the GPS catalog and the nearest time from the tremor catalog (Table 1). These time differences are in column 6 (Table 4). Every event in the GPS catalog has a match in the tremor catalog, except for the tremor event at 2010.15.

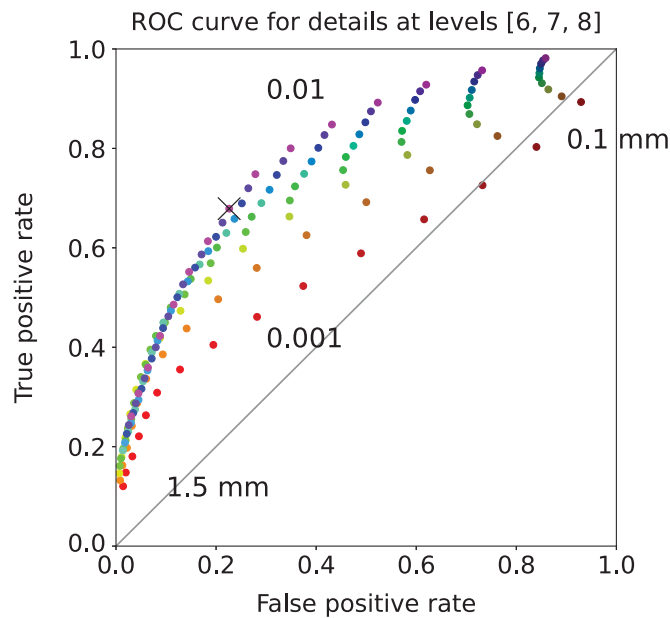


Figure 8. Receiver operating characteristic (ROC) curve for the sum of the 6th, 7th, and 8th level details of the wavelet decomposition. Each dot represents the true positive rate of event detections and the false positive rate of event detections for a given pair of thresholds (for the GPS and for the tremor). The black cross marks the true positive rate and the false positive rate obtained with the thresholds used to make Figure 9. The values of the threshold are color coded. The reds (bottom curve) correspond to the lowest value of the threshold for the tremor (0.001), whereas oranges, greens, blues, and purples correspond to increasing values of the threshold for the tremor (up to 0.01, top curve). The brightest colors (bottom left) correspond to the highest values of the threshold for the GPS (1.5 mm), whereas the darker colors (top right) correspond to decreasing values of the threshold for the GPS (0.1 mm).

There is also only one event in the tremor catalog that is not in the GPS catalog. It occurs at 2014.65 with a duration of 15 days and 190 hr of tremor. It occurs 0.25 yr after the nearest GPS event. There are also two marginal events in the tremor catalog with time differences of 0.13 and 0.10 yr, but those are also among the smaller events with 162 and 193 hr of tremor.

APPLICATION TO DATA FROM NEW ZEALAND

We now apply our wavelet-based method to detect slow slip events in New Zealand—a location where the spatial and temporal agreement between tremor and slow slip is not as good as in other subduction zones. The tectonics of the North Island of New Zealand are dominated by the westward subduction of the Pacific plate under the Australian plate at the Hikurangi trench. Two types of slow slip events have been observed at the Hikurangi margin. Shallow (10–15 km depth), shorter (1–3 weeks), and usually smaller (M_w 6.3–6.8) slow slip events have been observed every 18–24 months in the northern part of the margin. Deeper (35–60 km depth), longer (12–18 months), and larger (M_w 7.0) slow slip events have been observed every 5 yr in the southern part of the margin

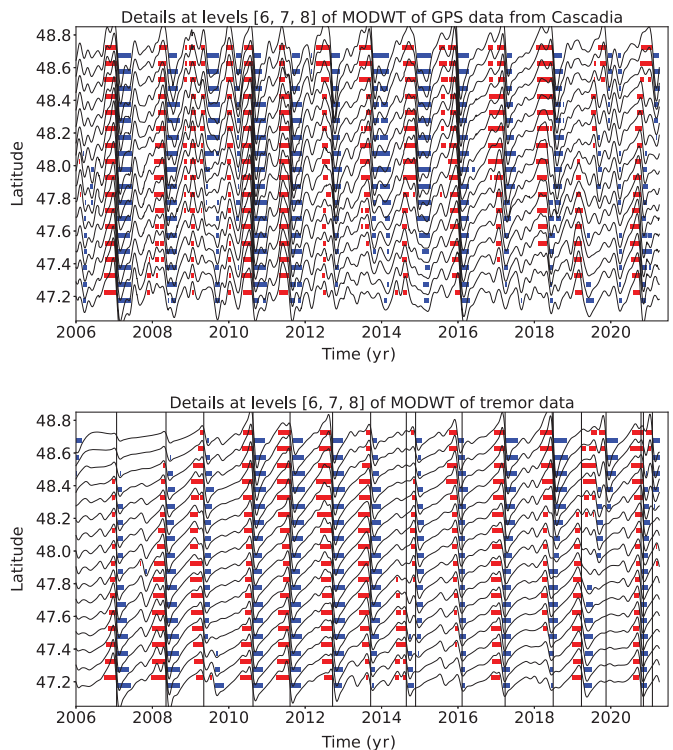


Figure 9. Top: Stacked sum of the 6th, 7th, and 8th levels details of the wavelet decomposition of the displacement over all the GPS stations located in a 50 km radius of a given point for the 16 red triangles indicated in Figure 3. Bottom: Sum of the 6th, 7th, and 8th levels detail multiplied by -1 of the cumulative tremor count in a 50 km radius of a given point for the same 16 locations. The black lines represent the timings of the ETS events from Table 1. We mark by a red rectangle every time in which the amplitude is higher than a threshold of 0.8 mm (for the GPS) or 0.01 (for the tremor that is about 56 times the average value of the signal). We mark by a blue rectangle every time in which the amplitude is lower than minus the threshold.

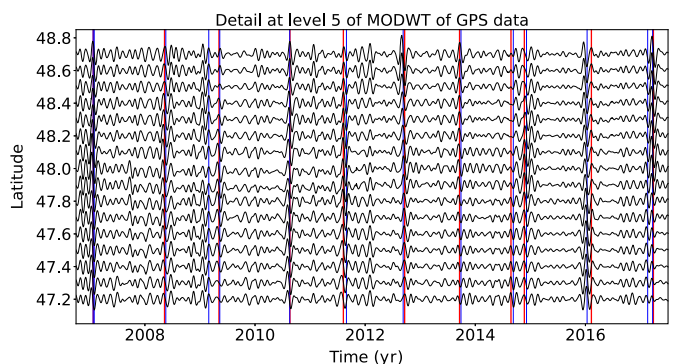


Figure 10. Top: Stacked 5th level details of the wavelet decomposition of the displacement over all the GPS stations located in a 50 km radius of a given point for the 16 red triangles indicated in Figure 3. The red lines represent the timings of the ETS events from Table 1. The blue lines represent the timings of the magnitude 5 events from the catalog of Michel *et al.* (2019). The color version of this figure is available only in the electronic edition.

TABLE 2
Magnitude 5–6 Events from Michel et al. (2019)

Time	Event Number	Magnitude	Subevent of Bigger Event
2007.06	1	5.64	Yes
2007.08	2	5.91	Yes
2008.38	11	5.50	Yes
2009.16	14	5.50	No
2009.36	17	5.32	Yes
2010.63	25	5.76	Yes
2011.66	31	5.61	Yes
2011.66	32	5.32	Yes
2012.69	35	5.56	Yes
2013.74	42	5.71	Yes
2014.69	49	5.31	Yes
2014.93	52	5.39	Yes
2016.03	57	5.80	Yes
2017.13	60	5.43	Yes
2017.22	61	5.37	Yes

TABLE 3
Number of GPS Stations Used for the Stacking for Each Location on Figure 3 and Number of Common Stations with the Location Immediately to the North and the Location Immediately to the South

Index	Latitude	Number of Stations	Common Stations (North)	Common Stations (South)
0	47.2	15	14	
1	47.3	18	17	14
2	47.4	24	20	17
3	47.5	21	20	20
4	47.6	22	14	20
5	47.7	17	12	14
6	47.8	13	8	12
7	47.9	10	9	8
8	48.0	10	7	9
9	48.1	8	7	7
10	48.2	10	8	7
11	48.3	9	9	8
12	48.4	9	5	9
13	48.5	7	5	5
14	48.6	6	5	5
15	48.7	5		5

(Wallace and Beavan, 2010; Todd and Schwartz, 2016). The detection of tremor has been elusive in northern Hikurangi. Delahaye et al. (2009) observed an increase in the rate of microseismicity down dip of the 2004 Gisborne slow slip event. More recently, however, (Kim et al., 2011) detected a low level of tremor activity that increased during the 2010 Gisborne slow slip event. As was the case for the microearthquakes, the source of the tremor was located down dip of the slow slip patch determined from GNSS data. Ide (2012) detected tremor down dip of the location of two deep slow slip events observed by

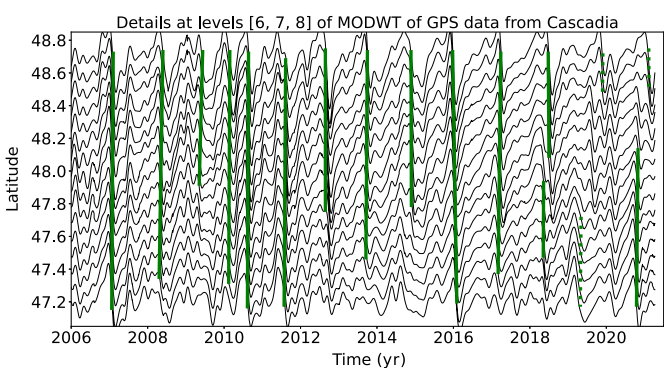


Figure 11. Same as top panel of Figure 9: Stacked sum of the 6th, 7th, and 8th levels details of the wavelet decomposition of the displacement over all the GPS stations located in a 50 km radius of a given point for the 16 red triangles indicated in Figure 3. We mark with a green bar the slow slip events from Table 4 detected with the wavelet method. Full lines correspond to robust detections (1 in Table 4) and dotted lines to less robust detections (2 in Table 4). The color version of this figure is available only in the electronic edition.

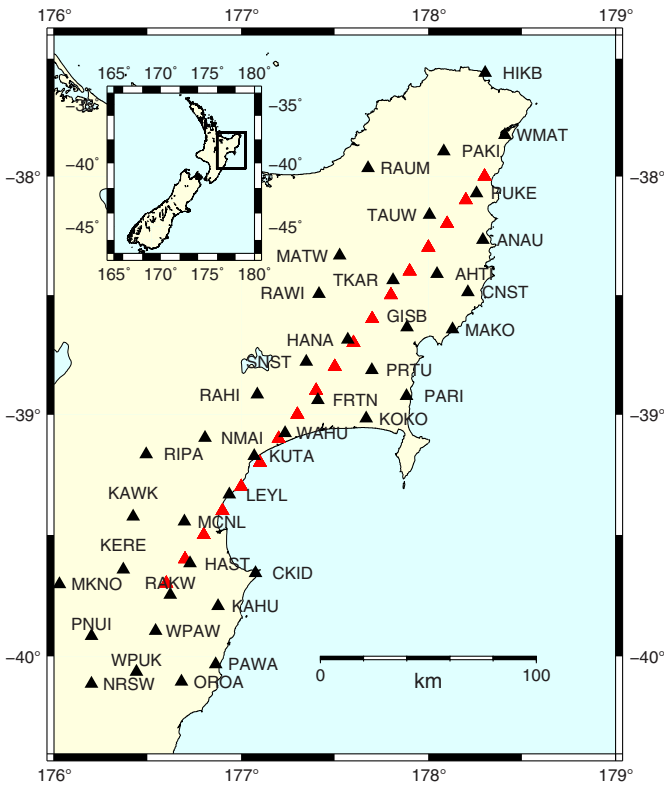



Figure 12. GPS stations used for the slow slip detection in New Zealand (black triangles). The red triangles are the locations where we stack the GPS data. They are located close to the 20 km depth contour of the plate boundary from Williams et al. (2013). The color version of this figure is available only in the electronic edition.

Wallace and Eberhart-Phillips (2013) in 2006 and 2008. However, contrary to ETS events in Cascadia and Nankai, the tremor activity did not seem to increase during the slow

TABLE 4

19 Cascadia Catalog of Slow Slip Events Based Only on MODWT Analysis of GPS Time Series and Inferring that the Transition of Red Followed Immediately by Blue Marks a Slow Slip Event

Start Time	End Time	Start Latitude	End Latitude		dT Tremor Catalog
2007.06	2007.10	47.16	48.72	1	0.02
2008.30	2008.40	47.35	48.73	1	0.01
2009.35	2009.44	47.92	48.73	1	0.05
2010.12	2010.15	47.32	48.73	1	0.50 no match
2010.61	2010.64	47.17	48.72	1	0.00
2011.57	2011.61	47.18	48.68	1	0.01
2012.65	2012.65	48.74	47.76	1	0.05
2013.71	2013.75	47.47	48.73	1	0.02
2014.89	2014.90	48.73	47.79	1	0.01
2015.98	2016.09	48.73	47.20	1	0.08
2017.17	2017.24	47.38	48.72	1	0.02
2018.35	2018.36	47.48	47.93	1	0.13 part of same event?
2018.48	2018.50	48.72	48.09	1	0.00
2019.32	2019.34	47.17	47.72	2	0.10
2019.90	2019.91	48.47	48.72	2	0.02
2020.79	2020.83	47.18	48.13	1	0.02 and 0.05
2021.11	2021.12	48.75	48.48	2	0.02

First four columns are the start and end times and start and end latitudes of the green bars in Figure 11. The fifth column is 1 for robust detection and 2 if not as robust. Column 6 is the time difference in years between the mid times of the GPS catalog and the nearest mid-times of the tremor catalog summarized in Table 1.

slip events. [Todd and Schwartz \(2016\)](#) detected tremor associated with most of the shallow slow slip events between 2010 and 2015, and located down-dip of the geodetically inferred slip area. They also detected deeper tremor between 20 and 50 km depth with unclear origin. They hypothesized that these tremor may be related to undetected deep long-term slow slip events.

To evaluate whether the wavelet analysis is effective in a region without robust tremor, we take all the New Zealand GPS stations located in a 50 km radius of a given location, for the 18 locations indicated in Figure 12, and we stack the 6th level details, the 7th level details, or the 8th level details over all the GPS stations. We then sum together the 6th, 7th, and 8th levels stacked wavelet details (Fig. 13, top panel). We highlight positive and negative peaks with red and blue colors, as was done in Figure 9. We cannot use the tremor data to decide what is the appropriate threshold above which we consider that there is a slow slip event. Slow slip events in New Zealand result in surface displacements that are similar in amplitude to twice as large as those observed in Cascadia. Therefore, the amplitudes of the peaks in the wavelet details should be similar in New Zealand and in Cascadia, and we choose identical thresholds for both the regions. Because a slow slip event in northern New Zealand results in a displacement in the east direction at the earth's surface, the slow slip events are indicated by a negative peak followed by a positive peak in the stacked wavelet details. We compare the results of the timings and the locations of the slow slip events to those events detected by [Todd and Schwartz \(2016\)](#). Because they only used data from five GPS stations (PUKE, ANAU, GISB, MAHI, and CKID), we indicate by a vertical orange bar on

the bottom panel of Figure 13 each time a slow slip event was detected for these stations. The orange bars are centered on the latitudes of the GPS stations. If a slow slip event was detected by more than one station, all the corresponding orange bars are linked together to show the spatial extent of the slow slip. [Todd and Schwartz \(2016\)](#) indicated by a question mark (on their Fig. 2 and their Table 1) additional possible events, and those are indicated by a dotted orange bar on Figure 13. To compare with the slow slip events detected with the wavelet method, we also mark by a green bar every time a negative peak lower than the threshold is followed by a positive peak higher than the threshold. Table 5 summarizes the slow slip events detected with the wavelet method for 2010–2016.

We observe that there is a good agreement between the events detected with the wavelet method and the events previously detected by [Todd and Schwartz \(2016\)](#). We clearly see an event propagating from south to north in January–February (event 2 from [Todd and Schwartz, 2016](#)), an event in March–April 2010 (event 3), an event in April–May 2011 in the northern part of the region studied (events 6 and 7), an event propagating south-to-north in August–September and September–October 2011 (events 8 and 9), and an event in December 2011 (event 10). Although [Todd and Schwartz \(2016\)](#) only detected this last event for GPS station GISB, it seems that this event may have also extended farther to the north and the south. We then clearly see an event in the northern part of the region studied in August 2012 (event 12), an event in December 2012–January 2013 (event 13), an event in the southern part of the region studied in February–March 2013 (event 14), an event propagating from south to north in

TABLE 5
20 New Zealand Catalog of Slow Slip Events for 2010–2016
Based Only on MODWT Analysis of GPS Time Series and
Inferring that the Transition of Red Followed Immediately
by Blue Marks a Slow Slip Event

Start Time	End Time	Start Latitude	End Latitude	
2010.05	2010.07	−39.67	−39.12	1
2010.19	2010.22	−39.12	−38.07	1
2010.75	2010.76	−39.73	−39.41	1
2011.36	2011.37	−38.22	−38.02	2
2011.71	2011.74	−37.97	−38.41	1
2011.67	2011.71	−39.73	−38.91	1
2011.92	2011.95	−38.84	−38.16	1
2012.63	2012.63	−39.42	−39.62	2
2012.64	2012.66	−38.53	−38.02	1
2012.95	2012.96	−38.32	−37.98	1
2013.15	2013.16	−38.87	−39.72	1
2013.55	2013.57	−38.62	−38.01	1
2013.74	2013.74	−38.77	−38.97	2
2013.92	2013.93	−38.17	−37.98	2
2013.91	2013.95	−39.37	−39.73	1
2014.78	2014.79	−38.03	−39.03	1
2014.96	2015.00	−39.07	−39.72	1
2015.53	2015.53	−39.42	−39.72	1
2015.52	2015.55	−37.97	−38.43	1
2015.78	2015.79	−38.77	−39.37	1

First four columns are the start and end times and start and end latitudes of the green bars in Figure 13. The fifth column is 1 for robust detection and 2 if not as robust.

June–July and July–August 2013 (events 15 and 16), an event in September 2014 (events 20 and 21), an event in the southern part of the region studied in December 2014–January 2015 (events 22 and 23), and an event in June–July 2015 in the northern part of the region studied (event 26). It is unclear if the event near station ANAU in early 2010 (event 1) is visible in the wavelet details, as it is too close to the beginning of the time series. The June–July 2010 event (event 4), the August 2010 event (event 5), and the March 2012 event (event 11) are not clearly visible in the wavelet details. The events in September–October 2013 (event 17), December 2013 (event 18), May–June 2014 (event 19), January–February (event 24), and February 2015 (events 25) are not clearly seen in the wavelet details, but there could be a small negative peak followed by a small positive peak at these times. In addition, there could be two other events that are not (Todd and Schwartz, 2016) in Fall 2010 (southern part of the region studied) and in Fall 2015.

Our wavelet-based method thus works well to detect transients in GPS data that could be slow slip events, even in the absence of tremor data. The choice of the appropriate threshold to decide that there is a transient, and the levels of the wavelet details that we look at for the detection may still not be easily made. There is a difference between Cascadia and New Zealand in terms of which wavelet details to stack. In particular, as there is more time between two slow slip events in New Zealand than in Cascadia, the biggest slow slip

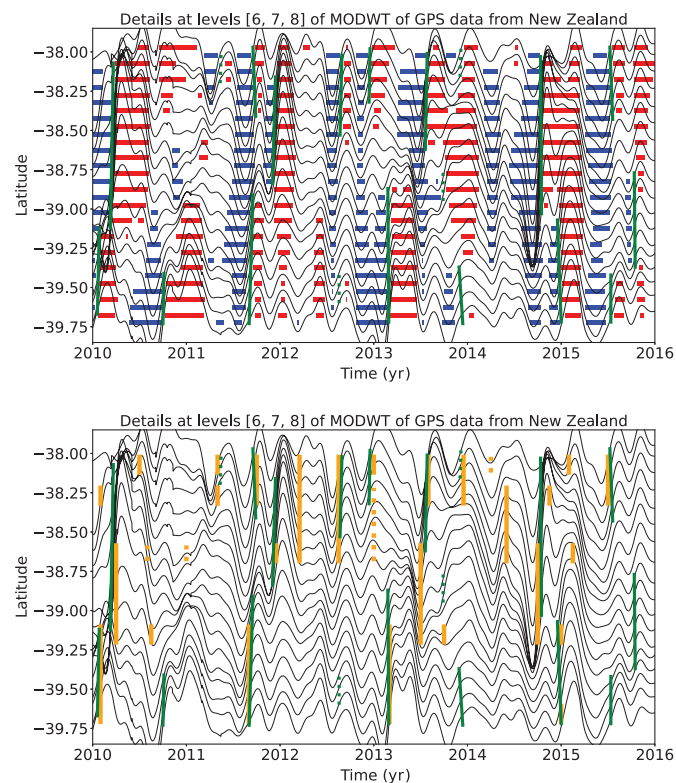


Figure 13. Top: Sum of the stacked 6th, 7th, and 8th level details of the wavelet decomposition of the displacement over all the GPS stations located in a 50 km radius of a given point for the 18 red triangles indicated in Figure 12. The time period covered is 2010–2016. We mark by a red rectangle every time in which the amplitude is higher than a threshold equal to 0.8 mm. We mark by a blue rectangle every time in which the amplitude is lower than minus the threshold. Bottom: Sum of the stacked 6th, 7th, and 8th level details of the wavelet decomposition. We mark with an orange bar the slow slip events detected by Todd and Schwartz (2016) and with a green bar the slow slip events from Table 5 detected with the wavelet method. Full lines correspond to robust detections (1 in Table 5) and dotted lines to less robust detections (2 in Table 5).

events (early 2010, late 2011, 2013, and late 2014) can also be seen on the 9th level detail for New Zealand, whereas they could not be seen for Cascadia. We then use the method to detect slow slip events during the period 2016–2022, which was not covered by Todd and Schwartz (2016) (Fig. 14). We note four large transients that could be slow slip events in late 2016, late 2017, early 2019 and mid-2021. There are also possible smaller events in the northern part of the area in mid-2018 and in the most of the areas studied in early 2020. Table 6 summarizes the slow slip events detected with the wavelet method for 2016–2022.

The method is thus applicable in regions where tremor data are not usable. To determine which wavelet levels to stack, we recommend analyzing each level detail. Look for spatially coherent patterns, wavelet details with energy at similar times, and high SNRs. Look for alternating positive and negative peaks that are consistent with the expected direction of slow

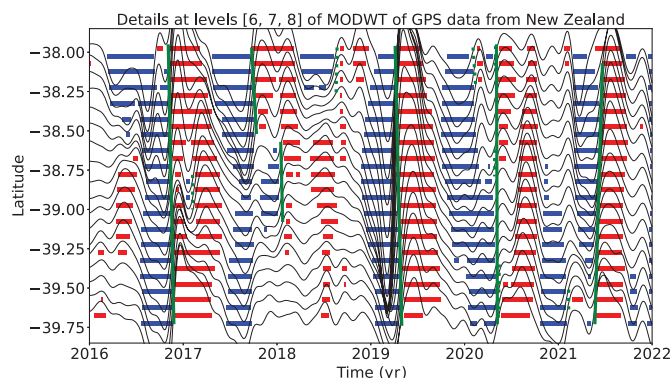


Figure 14. Top: Sum of the stacked 6th, 7th, and 8th level details of the wavelet decomposition of the displacement over all the GPS stations located in a 50 km radius of a given point for the 18 red triangles indicated in Figure 12. The time period covered in 2016–2022. We mark by a red rectangle every time in which the amplitude is higher than a threshold equal to 0.8 mm. We mark by a blue rectangle every time in which the amplitude is lower than minus the threshold. We mark with a green bar the slow slip events from Table 6 detected with the wavelet method. Full lines correspond to robust detections (1 in Table 6) and dotted lines to less robust detections (2 in Table 6).

slip. Consider wavelet details with time scales ranging from the expected duration of slow slip events to the expected recurrence times between slow slip events. For Cascadia and New Zealand, this would be weeks to years. Determination of a threshold is subjective. At large thresholds the large slow slip events should be clear. At smaller thresholds there is the possibility of identifying smaller events but at the risk of false detections.

CONCLUSION

In this article, we develop and test a new approach for detecting transient events in GPS time series, such as slow slip events. We used wavelet methods to analyze GNSS time series and tremor recordings of slow slip events in Cascadia and GNSS time series in New Zealand. We used detrended GNSS data, applied the MODWT transform, and stacked the wavelet details over several nearby GNSS stations. As an independent check on the timing of slow slip events, we also computed the cumulative number of tremor in the vicinity of the GNSS stations, detrended this signal, and applied the MODWT transform. In both the time series, we could then see simultaneous waveforms for which timing corresponds to the timing of slow slip events. We assumed that there is a slow slip event whenever the wavelet signal gets above a threshold. We verified that there is a good agreement between slow slip events detected with only GNSS data and slow slip events detected with only tremor data. The wavelet-based detection method detects all events of magnitude higher than 6 as determined by independent event catalogs (e.g., Michel *et al.*, 2019). We detected signals in the GPS data that could be magnitude 5 events, but it is

TABLE 6

New Zealand Catalog of Slow Slip Events for 2016–2022 Based Only on MODWT Analysis of GPS Time Series and Inferring that the Transition of Red Followed Immediately by Blue Marks a Slow Slip Event

Start Time	End Time	Start Latitude	End Latitude	
2016.84	2016.90	–37.96	–39.72	1
2017.10	2017.10	–38.78	–39.00	2
2017.73	2017.78	–37.98	–38.51	1
2018.04	2018.06	–38.58	–39.07	1
2018.63	2018.64	–38.27	–37.97	2
2019.26	2019.33	–37.97	–39.73	1
2020.09	2020.12	–37.97	–38.23	2
2020.34	2020.35	–37.96	–39.72	1
2020.33	2020.33	–37.96	–38.10	2
2020.32	2020.32	–38.62	–38.79	2
2020.36	2020.37	–39.70	–39.35	2
2021.11	2021.11	–39.51	–39.64	2
2021.39	2021.47	–39.72	–38.08	1

First four columns are the start and end times and start and end latitudes of the green bars in Figure 13. The fifth column is 1 for robust detection and 2 if not as robust.

not easy to differentiate between robust detections and false detections. We then applied the method to GNSS data in New Zealand and detected slow slip events consistent with the events previously detected by Todd and Schwartz (2016).

DATA AND RESOURCES

The Global Positioning System (GPS) recordings used for this analysis can be downloaded from the Pacific Northwest Geodetic Array (PANGA) website Global Navigation Satellite Systems (GPS/GNSS Network and Geodesy Laboratory: Central Washington University, Other/Seismic Network, 1996) <http://www.pnw.cwu.edu/> and the Geonet website <https://www.geonet.org.nz/>. The Python scripts used to analyze the data and make the figures can be found on the first author's Github account <https://github.com/ArianeDucellier/slowslip>. Figures 3 and 12 were created using Generic Mapping Tool (GMT; Wessel and Smith, 1991). The supplemental material includes three figures showing the effects of boundary conditions, missing data and common modes, and a figure showing four additional small displacements detected in the GPS data.

DECLARATION OF COMPETING INTERESTS

The authors acknowledge that there are no conflicts of interest recorded.

ACKNOWLEDGMENTS

The authors would like to thank two anonymous reviewers: the Associate Editor Jeanne Hardebeck and the Editor-in-Chief P. Martin Mai; their comments greatly helped improve the article. This work was funded by the grant from the National Science Foundation EAR-1358512. Ariane Ducellier would like to thank Professor Donald Percival for introducing her to wavelet methods during his excellent class on Wavelets: Data Analysis, Algorithms, and Theory taught at University of Washington.

REFERENCES

- Aguiar, A., T. Melbourne, and C. Scrivner (2009). Moment release rate of Cascadia tremor constrained by GPS, *J. Geophys. Res.* **114**, no. B7, doi: [10.1029/2008JB005909](https://doi.org/10.1029/2008JB005909).
- Alba, S., R. J. Weldon, D. Livelybrooks, and D. A. Schmidt (2019). Cascadia ETS events seen in tidal records (1980–2011), *Bull. Seismol. Soc. Am.* **109**, no. 2, 812–821.
- Audet, P., and Y. Kim (2016). Teleseismic constraints on the geological environment of deep episodic slow earthquakes in subduction zone forearcs: A review, *Tectonophysics* **670**, 1–15.
- Bartlow, N. M. (2020). A long-term view of episodic tremor and slip in Cascadia, *Geophys. Res. Lett.* **43**, no. 3, e2019GL085303.
- Beroza, G., and S. Ide (2011). Slow earthquakes and nonvolcanic tremor, *Annu. Rev. Earth Planet. Sci.* **39**, 271–296.
- Delahaye, E., J. Townend, M. Reyners, and G. Rogers (2009). Microseismicity but no tremor accompanying slow slip in the Hikurangi subduction zone, New Zealand, *Earth Planet. Sci. Lett.* **277**, 21–28.
- Frank, W. (2016). Slow slip hidden in the noise: The intermittence of tectonic release, *Geophys. Res. Lett.* **43**, 10,125–10,133.
- 13** GPS/GNSS Network and Geodesy Laboratory: Central Washington University, Other/Seismic Network (1996). Pacific Northwest Geodetic Array (PANGA), available at <http://www.pnwgeodetic.org/cwu.edu/>.
- Hall, K., H. Houston, and D. Schmidt (2018). Spatial comparisons of tremor and slow slip as a constraint on fault strength in the northern Cascadia subduction zone, *Geochem. Geophys. Geosys.* **19**, no. 8, 2706–2718.
- Hawthorne, J. C., and A. M. Rubin (2013). Short-time scale correlation between slow slip and tremor in Cascadia, *J. Geophys. Res.* **118**, 1316–1329.
- Hiramatsu, Y., T. Watanabe, and K. Obara (2008). Deep low-frequency tremors as a proxy for slip monitoring at plate interface, *Geophys. Res. Lett.* **35**, L13304.
- Ide, S. (2012). Variety and spatial heterogeneity of tectonic tremor worldwide, *J. Geophys. Res.* **117**, no. B3, doi: [10.1029/2011JB008840](https://doi.org/10.1029/2011JB008840).
- Jiang, Y., S. Wdowinski, T. H. Dixon, M. Hackl, M. Protti, and V. Gonzalez (2012). Slow slip events in Costa Rica detected by continuous GPS observations, 2002–2011, *Geochem. Geophys. Geosys.* **13**, Q04006.
- Kim, M., S. Schwartz, and S. Bannister (2011). Non-volcanic tremor associated with the March 2010 Gisborne slow slip event at the Hikurangi subduction margin, New Zealand, *Geophys. Res. Lett.* **38**, L14301.
- Kumar, P., and E. Foufoula-Georgiou (1997). Wavelet analysis for geophysical applications, *Rev. Geophys.* **35**, no. 4, 385–412.
- Li, S., J. Freymueller, and R. McCaffrey (2016). Slow slip events and time-dependent variations in locking beneath lower Cook inlet of the Alaska-Aleutian subduction zone, *J. Geophys. Res.* **121**, 1060–1079.
- Michel, S., A. Gualandi, and J.-P. Avouac (2019). Interseismic coupling and slow slip events on the Cascadia megathrust, *Pure Appl. Geophys.* **176**, 3867–3891.
- Nishimura, T., T. Matsuzawa, and K. Obara (2013). Detection of short-term slow slip events along the Nankai trough, southwest Japan, using GNSS data, *J. Geophys. Res.* **118**, 3112–3125.
- Nuyen, C. P., and D. A. Schmidt (2021). Filling the gap in Cascadia: The emergence of low-amplitude long-term slow slip, *Geochem. Geophys. Geosys.* **22**, no. 3, e2020GC009477.
- Obara, K., H. Hirose, F. Yamamizu, and K. Kasahara (2004). Episodic slow slip events accompanied by non-volcanic tremors in southwest Japan subduction zone, *Geophys. Res. Lett.* **31**, L23602.
- Ohtani, R., J. McGuire, and P. Segall (2010). Network strain filter: A new tool for monitoring and detecting transient deformation signals in GPS arrays, *J. Geophys. Res.* **115**, no. B12, doi: [10.1029/2010JB007442](https://doi.org/10.1029/2010JB007442).
- Percival, D., and A. Walden (2000). Wavelet methods for time series analysis, in *Cambridge Series in Statistical and Probabilistic Mathematics*, Cambridge University Press, New York, New York, U.S.A..
- Preston, L., K. Creager, R. Crosson, T. Brocher, and A. Trehu (2003). Intralab earthquakes: Dehydration of the Cascadia slab, *Science* **302**, 1197–1200.
- Radiguet, M., F. Cotton, M. Vergnolle, M. Campillo, A. Walpersdorf, N. Cotte, and V. Kostoglodov (2012). Slow slip events and strain accumulation in the Guerrero gap, Mexico, *J. Geophys. Res.* **117**, no. B4, doi: [10.1029/2011JB008801](https://doi.org/10.1029/2011JB008801).
- Rogers, G., and H. Dragert (2003). Tremor and slip on the Cascadia subduction zone: The chatter of silent slip, *Science* **300**, no. 5627, 1942–1943.
- Schmidt, D. A., and H. Gao (2010). Source parameters and time-dependent slip distributions of slow slip events on the Cascadia subduction zone from 1998 to 2008, *J. Geophys. Res.* **115**, no. B4, doi: [10.1029/2008JB006045](https://doi.org/10.1029/2008JB006045).
- Shelly, D., G. Beroza, and S. Ide (2007). Non-volcanic tremor and low-frequency earthquake swarms, *Nature* **446**, 305–307.
- Szeliga, W., T. Melbourne, M. Miller, and V. Santillan (2004). Southern Cascadia episodic slow earthquakes, *Geophys. Res. Lett.* **31**, L16602.
- Szeliga, W., T. Melbourne, M. Santillan, and M. Miller (2008). GPS constraints on 34 slow slip events within the Cascadia subduction zone, 1997–2005, *J. Geophys. Res.* **113**, no. B4, doi: [10.1029/2007JB004948](https://doi.org/10.1029/2007JB004948).
- Todd, E., and S. Schwartz (2016). Tectonic tremor along the northern Hikurangi margin, New Zealand, between 2010 and 2015, *J. Geophys. Res.* **121**, 8706–8719.
- Vergnolle, M., A. Walpersdorf, V. Kostoglodov, P. Tregoning, J. A. Santiago, N. Cotte, and S. I. Franco (2010). Slow slip events in Mexico revised from the processing of 11 year GPS observations, *J. Geophys. Res.* **115**, no. B8, doi: [10.1029/2009JB006852](https://doi.org/10.1029/2009JB006852).
- Wallace, L. M. (2020). Slow slip events in New Zealand, *Annu. Rev. Earth Planet. Sci.* **48**, 175–203.
- Wallace, L., and J. Beavan (2010). Diverse slow slip behavior at the Hikurangi subduction margin, New Zealand, *J. Geophys. Res.* **115**, no. B12, doi: [10.1029/2010JB007717](https://doi.org/10.1029/2010JB007717).
- Wallace, L., and D. Eberhart-Phillips (2013). Newly observed, deep slow slip events at the central Hikurangi margin, New Zealand: Implications for downdip variability of slow slip and tremor, and relationship to seismic structure, *Geophys. Res. Lett.* **40**, 5393–5398.
- Wallace, L. M., J. Beavan, S. Bannister, and C. Williams (2012). Simultaneous long-term and short-term slow slip events at the Hikurangi subduction margin, New Zealand: Implications for processes that control slow slip event occurrence, duration, and migration, *J. Geophys. Res.* **117**, no. B11, doi: [10.1029/2012JB009489](https://doi.org/10.1029/2012JB009489).
- Wech, A. (2010). Interactive tremor monitoring, *Seismol. Res. Lett.* **81**, no. 4, 664–669.

- Wech, A. (2016). Extending Alaska's plate boundary; tectonic tremor generated by Yakutat subduction, *Geology* **44**, no. 7, 587–590.
- Wei, M., J. McGuire, and E. Richardson (2012). A slow slip event in the south central Alaska subduction zone, *Geophys. Res. Lett.* **39**, L15309.
- Wessel, P., and W. H. F. Smith (1991). Free software helps map and display data, *Eos Trans. AGU* **72**, 445–446.
- Williams, C. A., D. Eberhart-Phillips, S. Bannister, D. H. Barker, S. Henrys, M. Reyners, and R. Sutherland (2013). Revised interface geometry for the Hikurangi subduction zone, New Zealand, *Seismol. Res. Lett.* **84**, no. 6, 1066–1073.
-

Manuscript received 3 November 2021

Queries

1. AU: As per SSA style, the abbreviation “(NSF)” has been deleted because it is not used again in this article.
2. AU: SSA reserves “while” to describe events that happen simultaneously. When this is not the case, “while” has been changed to “although” or “whereas” throughout. Please provide revisions if necessary.
3. AU: SSA tries to avoid using a slash in nonmathematical contexts. Please provide alternative wording for “Jet Propulsion Laboratory/NASA.”
4. AU: In your inline equation: Does the asterisk represent (1) multiplication (so would be replaced by a multiplication sign or closed up, whichever you prefer), (2) convolution in cross correlation (in which the asterisk would be centered), or (3) a complex conjugate of a complex number (in which the asterisk would be set as a superscript)?
5. AU: Throughout the article: please review whether the mathematical terms and equations were edited as per your meaning. Kindly amend if required.
6. AU: SSA uses “because” instead of “since” or “as” unless they are intended to refer to time or specific mathematical conditions. Would it be consistent with your meaning here to change “since” to “because”?
7. AU: SSA style avoids using “above” and “below” when referring to other parts of the same paper. Please review the edit to the text and provide alternative wording if needed.
8. AU: Should this be transition than transient? Kindly verify for its intended meaning.
9. AU: Should this be transition than transient? Kindly verify for its intended meaning.
10. AU: Please verify whether your meaning of the Sentence “To convert our filtered...” is clear. Kindly verify and amend if required.
11. AU: Should this be transition than transient? Kindly verify for its intended meaning.
12. AU: Please provide the last accessed month and year for all the URLs.
13. AU: Please provide last accessed date and year for reference GPS/GNSS Network and Geodesy Laboratory: Central Washington University, Other/Seismic Network (1996).
14. AU: Please provide editor name for reference Percival and Walden (2000).
15. AU: Please note that figure legends and axis labels are edited to match the SSA style and to be consistent with the text. Please verify the changes and confirm whether the changes do not affect your intended meaning.
16. AU: In Figure 12 caption: Please check and provide the Inset figure description if required.
17. AU: The set up of Tables 1 to 6 have been changed to conform with SSA style. Please check that your meaning was retained.
18. AU: Please indicate if the roman capital M throughout the Tables should be changed to (1) bold M or (2) M_w (italic “M” and subscript roman “w”).
19. AU: Please provide the 5th column header for Table 4.
20. AU: Please provide the 5th column header for Table 5.
21. AU: Please provide the 5th column header for Table 6.